Modeling of a linear motor feed drive including pre-rolling friction and aperiodic cogging and ripple

Fernando J. Villegas, Rogelio L. Hecker, Miguel E. Peña, Diego A. Vicente & Gustavo M. Flores

The International Journal of Advanced Manufacturing Technology

ISSN 0268-3768

Int J Adv Manuf Technol
DOI 10.1007/s00170-014-5795-6

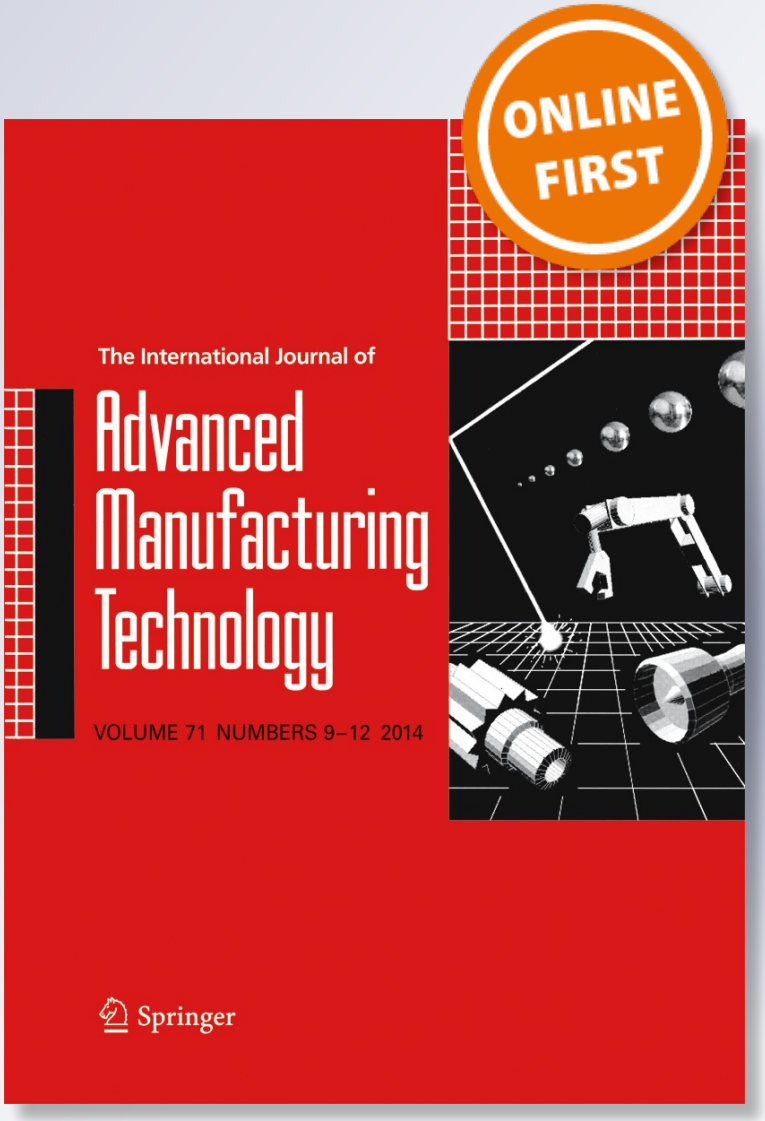

Springer

Int J Adv Manuf Technol
DOI 10.1007/s00170-014-5795-6

ORIGINAL ARTICLE

Modeling of a linear motor feed drive including pre-rolling friction and aperiodic cogging and ripple

Fernando J. Villegas · Rogelio L. Hecker · Miguel E. Peña · Diego A. Vicente · Gustavo M. Flores

Received: 16 February 2013 / Accepted: 17 March 2014

Abstract This work addresses the systematic modeling of a linear feed drive based on a linear synchronous motor, a helpful step in control design for precise machine tools using linear motors. The model considers the electrical dynamics, ripple, cogging effects, and friction. For ripple and cogging, periodic and aperiodic behaviors are analyzed, and simple models are proposed to reflect the observed behavior. Friction is represented by the generalized Maxwell-slip model Al-Bender (IEEE Trans Autom Control 50:1883–1887, 2005), and the particular manner in which pre-rolling parameters and Stribeck curve were determined for the current system is shown here for completeness. Finally, the model shows a good performance both in simulation and feedforward control.

Keywords Linear motor · Feed drive · Modeling · Ripple · Cogging · Friction

1 Introduction

Linear motors are an attractive alternative for machine tool feed drives due to their high speed and acceleration capability without the limitations coming from vibration modes typical of ball-screw drives [8]. However, unlike ball-screw drives where mechanical coupling provides certain degree of robustness, linear motors are more sensitive to force disturbances. Thus, for design and simulation of a control strategy, it is convenient to have a model containing as much information as possible about these forces. This includes the consideration of pre-rolling friction, which has a major role on motion reversal error [19, 26].

There are several works which address to some extent the modeling of certain types of linear motors. One such model is shown in [18] although the motor model neglects the electrical dynamics. In addition, it only considers a simple model for friction, which is represented as pure viscous friction. Furthermore, ripple and cogging are strictly periodic with position and can be represented by just two harmonics. More detailed friction models are considered in [5, 6, 25], which have been employed for control purposes in several works, such as [22–24]. However, these friction models are still static and cannot describe pre-rolling friction. Besides, cogging is represented by a single dominant spatial frequency sinusoid. A motor model which takes pre-rolling friction into account is shown in [10]. However, in this case, modeling and identification are performed for a linear motor in which force ripple and cogging force are not an issue. In [29], a model for a linear motor that includes these effects is given in the context of a drive used in a grinding process. Nevertheless, it does not take into account the electrical dynamics. It also uses the simple cogging and ripple model shown in [18]. A model which considers the electrical dynamics in some detail is given in [9] although the friction model employed does not account for pre-rolling friction and force ripple is not considered.

In the present work, a model of a linear motor feed drive based on a permanent magnet linear synchronous motor (PMLSM) is shown. This model considers the electrical

F. J. Villegas · R. L. Hecker (✉)
Universidad Nacional de La Pampa—CONICET,
Calle 110 Nro. 390, General Pico 6360, La Pampa, Argentina
e-mail: hecker@ing.unlpam.edu.ar

D. A. Vicente · G. M. Flores
Universidad Nacional de La Pampa, General Pico 6360,
La Pampa, Argentina

M. E. Peña
Instituto de Automática, Universidad Nacional de San Juan,
San Juan 5400, San Juan, Argentina

Published online: 15 April 2014

dynamics of the current loop, motor inertia, friction force, ripple, and cogging force in a level of detail subsequently described. As done in [10], the electrical dynamics is modeled by a transfer function. Friction will be represented by the Generalized Maxwell-slip (GMS) model, which has been successfully used to describe friction on rotative ball bearings outperforming other models such as LuGre [27]. As for cogging and ripple, instead of adapting an existing model to describe these effects, their dependence with position will be determined first. The periodic and aperiodic characteristics of these curves are then analyzed and a suitable model is proposed.

Section 2.1 describes the actual system used for experimentation as well as an overview of the complete model. The order of the following sections approximately resembles the order in which the model parameters were determined for the actual system. The transfer function chosen to approximate the dynamics of the current loop is detailed in Section 2.2. The terms involving cogging force and force ripple are studied in Section 2.3 where a suitable model is proposed. Section 2.4 is devoted to friction, beginning with a review of the characteristics of the model as presented by [11] and followed by the results of the determination of the model parameters for the actual system. Then, simulation of the motor behavior under closed loop control is compared to the actual motion in Section 3, where the impact of simplifying particular parts of the model is also shown. In Section 4, the performance of the model in feedforward control is also shown. The paper finally ends with conclusions in Section 5.

2 Model

2.1 System description

The experimental setup includes a permanent magnet linear synchronous motor (PMLSM) and a current amplifier. The motor consists of a forcer with an iron-core three-phase winding and a reaction rail composed of a steel base plate with permanent magnets. The linear stage, shown in Fig. 1, is composed of a base plate attached to the motor reaction rail and ball guide rails and a slide attached to the motor forcer. The slide moves over the ball guide rails on the base by means of four ball runner blocks with 8 % preload.

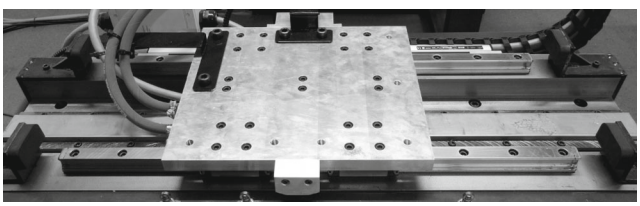

Fig. 1 Linear motor stage

The setup also includes a linear scale which provides position feedback both for the current amplifier and for the measurements performed in this work, with a resolution of 100 nm.

A block diagram for the model of the linear motor is shown in Fig. 2, where $G(s)$ approximates the electrical dynamics and its order as well as its parameters will result from identification.

The output of the block $K_f(x)$ represents the force developed by the motor for a particular current and is dependent on the forcer position due to the ripple effect [20]. The block $F_{\mathrm{cg}}(x)$ is related to the cogging force, which is also position-dependent. Finally, the block F_f represents the friction force and it is described by the GMS model [11]. It is assumed that variations of the friction model parameters along the motion range can be neglected. The motion equation is then given by

$$K_f(x)i(t) - F_{\mathrm{cg}}(x) - F_f(t,\dot{x}) - F_e(t) = m\ddot{x} \tag{1}$$

where x represents the position of the moving part and F_e accounts for the external forces not included in the other terms. Initially, no assumptions will be made about the nature of $K_f(x)$ and $F_{\mathrm{cg}}(x)$ besides their static dependence on position.

2.2 Current loop identification

In contrast to other works where the input of the system is the motor terminal voltage, such as in [25], the input to the present system is the reference input of a current controller. Thus, for the present system, the electrical dynamics corresponds to the dynamics from the amplifier reference input to the motor current. For the system considered, that input determines the reference to a PI controller which drives a voltage source inverter acting on the motor three-phase winding. The electrical dynamics will be modeled using the same approach used in [31] for a rotary motor and in [10] for a linear motor that is the approximation of the current loop dynamics by a transfer function. Although the present work

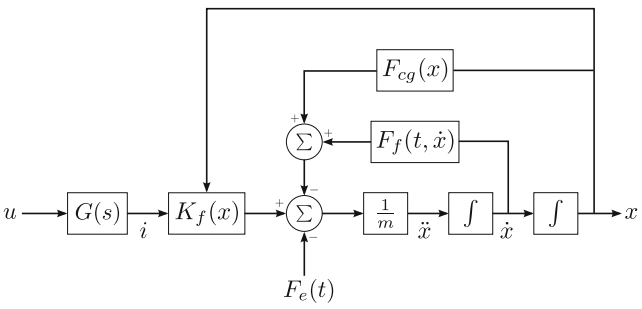

Fig. 2 Proposed linear motor model

follows the same approach than the aforementioned references, a description of the signals used and results obtained is given here for completeness of the whole model.

The experiment consists on applying a suitable voltage signal as a reference input to the current amplifier and registering the corresponding feedback current output at a sampling time of 500 ∞s. From the different signals used, the model has been identified using a maximum length pseudo-random binary signal of order 11. Also, several model structures with orders ranging from 1 to 5 were fitted to the data, from which a second order ARMAX model has been selected. From the data fit and compensating for the measurement delay on the digitized output, the resulting pulse transfer function from voltage reference to motor current is given by

$$G(z) = \frac{0.057909(z + 0.7461)}{z(z^2 - 1.404z + 0.4938)} \tag{2}$$

corresponding to a pure delay of one sample and a continuous transfer function with complex conjugate poles at 112Hz. Figure 3 shows the behavior of the model in comparison with the real output.

2.3 Cogging force and force ripple model

Cogging force and force ripple are described in several works, including [18, 29]. Force ripple is an electromagnetic effect by which the motor force constant varies with position and is represented by periodic functions in [3, 20, 32].

Cogging force, on the other hand, results from the attraction between the ferromagnetic core of motor windings and the permanent magnets on the reaction rail. This is a force varying with forcer position and exists even when the motor is not energized. Cogging force is frequently described as a periodic function of forcer position, such as in [3, 5, 6, 22–25, 30, 32, 33, 35]. However, it may exhibit aperiodic behavior, as shown in [16] where cogging force is modeled as a sum of sines and cosines of varying amplitude along the motor stroke. The varying amplitude is represented by B-spline functions, and the model shows good agreement to the measured curve. However, the model may require a large number of parameters, depending on the number of harmonics considered, the order of the spline, and the number of magnet segments on the motor axis.

In the present work, the dependence of both effects with position is determined, and the periodic and aperiodic characteristics of these curves are analyzed. Then, a model is proposed in order to obtain a reasonable agreement with a few parameters.

2.3.1 Measurement

The present work uses the setup shown in Fig. 4 to perform closed loop motions at low velocity for different constant loads as in [20]. However, instead of fitting a periodic model, in this work, ripple and cogging curves for the whole position range will be obtained to analyze their periodic and aperiodic behavior. Also, the ripple effect is represented here by the position-varying force constant $K_f(x)$.

Considering the motor Eq. (1) for steady-state motion, P being the load transmitted by the pulley mechanism and $I(x, v, P)$ the corresponding motor current, this equation can be expressed for positive and negative speeds of magnitude $v > 0$ as

$$\begin{aligned} K_f(x)I(x, v, P) &= F_f(v) + F_{cg}(x) + P \\ K_f(x)I(x, -v, P) &= -F_f(v) + F_{cg}(x) + P \end{aligned} \tag{3}$$

by considering the odd symmetry of the static relationship between steady-state velocity and friction force according to the friction model.

Then, from a group of displacements at constant speed v in both directions although with different constant forces P_1 and P_2 results that

$$K_f(x) = 2\frac{P_1 - P_2}{I(x, v, P_1) + I(x, -v, P_1) - I(x, -v, P_2) - I(x, v, P_2)} \tag{4}$$

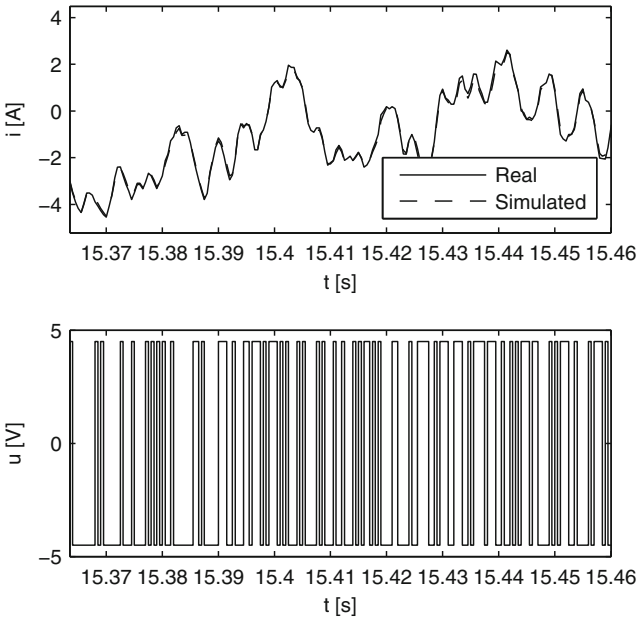

Fig. 3 Simulated and measured feedback current output

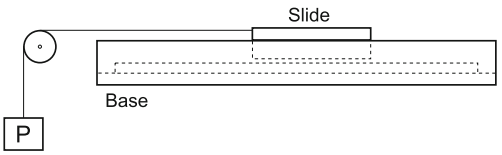

Fig. 4 Setup for cogging and ripple determination

Once $K_f(x)$ is known, $F_{cg}(x)$ can be easily calculated. One way to do this is through motions at constant speed v in both directions with a load P in which case this function can be determined as follows

$$F_{cg}(x) = \frac{K_f(x)}{2}(I(x, v, P) + I(x, -v, P)) - P \tag{5}$$

It should be noted that this procedure may result in the term $F_{cg}(x)$ including other forces not depending on velocity, such as a constant term when the motor is not horizontal or a varying term when sealing bellows are present. In such a case, the modeling of these additional forces will also be included in the term $F_{cg}(x)$.

For the actual system, six movements were performed at a constant speed of 1 mm/s in both directions. For one pair of motions, there is an applied load of 54.9 N while on other there is a load of 272.7 N. The remaining pair of motions is performed without load. For the whole group of experiments, the corresponding current is linearly interpolated to the same set of position points x_i, obtaining for every motion the function $I(x_i, v, P)$. Figure 5 shows the curves for $K_f(x_i)$ and $F_{cg}(x_i)$.

2.3.2 Model

The sequences F_{cg} and K_f were previously obtained for a uniform sampling of the position range of interest. As a way to assess its periodic and aperiodic behaviors, this work considers the local variations in frequency content along the position range. In order to gain insight about the position-varying spectral characteristics for both terms, the discrete short time Fourier transforms [17] (DSTFT) $X_F(n, k)$ for $F_{cg}(n)$ and $X_K(n, k)$ for $K_f(n)$ are considered. The sample index n is related to position as $x = nL_s$ for a sampling of $L_s = 0.1$ mm, and the frequency index k corresponds to a spatial frequency of $f_k = 1/\lambda_k = k/(NL_s)$ where the frequency sampling factor is $N = 750$. The DSTFT is performed with a rectangular window of 750 samples, corresponding to a period of 75 mm, i.e., the distance between pairs of magnets. Figures 6a and 8a show the superposition of several frequency plots of $|X_F|/N$ and $|X_K|/N$ for different position values. For convenience, the values shown on the frequency axis are actually the spatial wavelengths λ_k for the corresponding frequencies f_k.

Figure 6a shows clear peaks for wavelengths of 37.5, 18.75, and 12.5 mm. Furthermore, magnitude and phase for these wavelengths seem to remain approximately constant, as shown in Fig. 7. Therefore, these components account for the periodic behavior in $F_{cg}(x)$ and will be modeled by sinusoidal functions of constant amplitude and phase.

On the other hand, the zero-frequency term undergoes a significant change with position as can be seen in Fig. 6b, introducing aperiodic behavior in $F_{cg}(x)$. In order to obtain a linearly parameterizable approximation of $F_{cg}(x)$, a third order polynomial has been used to represent the variation of this term.

Then, $F_{cg}(x)$ has been fitted to the following expression

$$F_{cg}(x) = \sum_{k=0}^{3} c_k x^k + \sum_{k=1}^{3} \left(a_k \cos\left(\frac{2\pi kx}{37.5}\right) + b_k \sin\left(\frac{2\pi kx}{37.5}\right)\right) \tag{6}$$

The same criteria are employed to construct the simplified model of $K_f(x)$ (Fig. 8) except that the 25 mm harmonic, although similar in magnitude to the 18.75 mm one at the extremes of the position range, is not included. This could result in a worst agreement at the ends of the motor path, but it allows to avoid the significant increase in the number of parameters that would be required to describe this varying amplitude and varying phase term, which can be seen in Fig. 9. Then, the harmonics considered are again

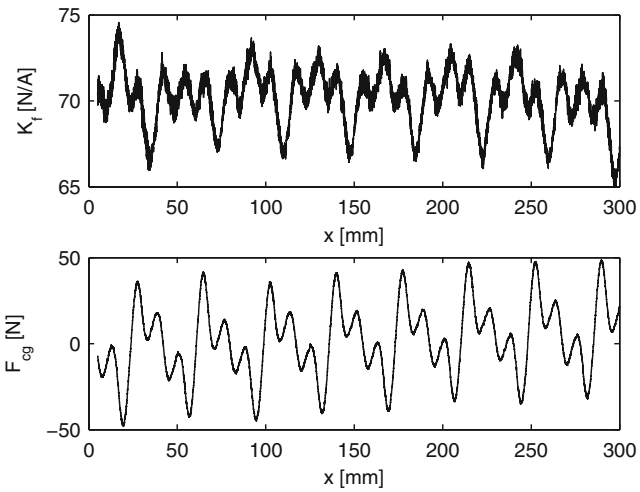

Fig. 5 Force ripple and cogging force

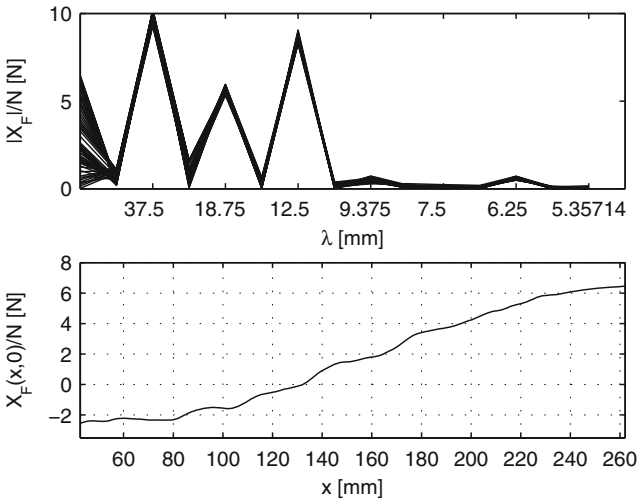

Fig. 6 Plots from DSTFT of $F_{cg}(x)$

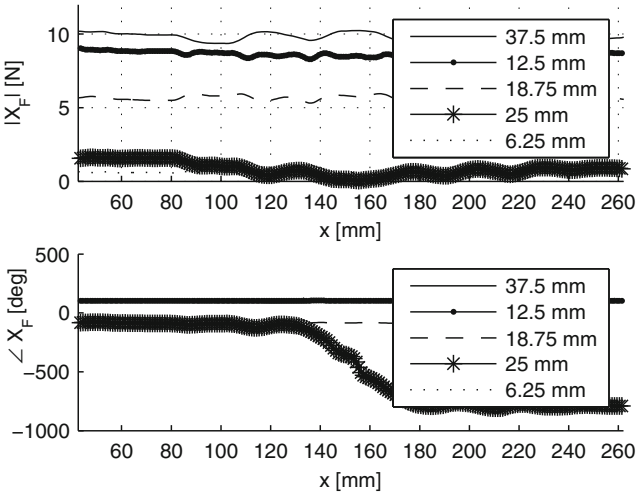

Fig. 7 Magnitude and unwrapped phase of X_F for several wavelengths

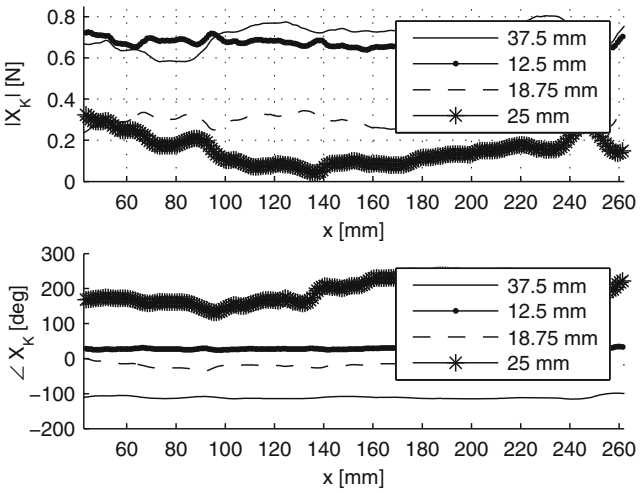

Fig. 9 Magnitude and unwrapped phase of X_K for several wavelengths

those with wavelengths of 37.5, 18.75, and 12.5 mm, which are approximated once more by sinusoidal terms of constant amplitude and phase. Figure 8b shows a small variation of the zero-frequency term except at the end of stroke. This variation has been considered on the model and the curve determined for $K_f(x)$ has been fitted to the following expression

$$K_f(x) = \sum_{k=0}^{2} c_k x^k + \sum_{k=1}^{3} \left(a_k \cos\left(\frac{2\pi k x}{37.5}\right) + b_k \sin\left(\frac{2\pi k x}{37.5}\right)\right) \tag{7}$$

To sum up, the simplified models for $F_{cg}(x)$ and $K_f(x)$ consist on Fourier polynomials with a fundamental period equal to the distance between magnets (37.5 mm for the current system) added to appropriate functions. The added function is a third degree polynomial for the case of $F_{cg}(x)$ and a second degree polynomial for the case of $K_f(x)$. Being these parameterizations linear on the parameters, the data fitting is performed by a simple linear regression, obtaining the parameters shown on Table 1. The comparison between real and fitted curves is shown in Fig. 10. It is worth mentioning that a model considering only the periodic part would have increased the rms error in a 93.8 % for $F_{cg}(x)$ and 13.6 % for $K_f(x)$.

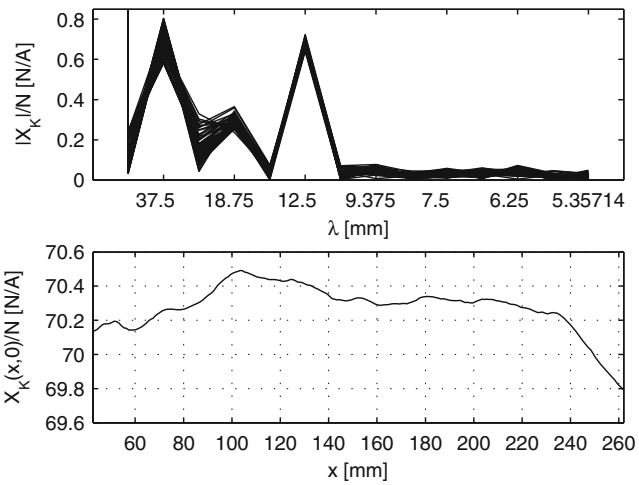

Fig. 8 Plots from DSTFT of $K_f(x)$

2.4 Friction model

There is a number of models capable of representing friction behavior to some extent. A model which has been widely used is the LuGre model [4], a single-state dynamic model which captures most of the observed phenomena and has already been used to model friction on linear motors in [29]. However, it cannot reproduce accurately the non-local memory characteristics of pre-sliding friction [11] and, under certain conditions, may even exhibit steady-state motion below breakaway force [7]. To overcome these issues, several other models have been proposed, such as the elasto-plastic friction model [7], the Leuven model

Table 1 Ripple and cogging force parameters

	c_0	c_1	c_2	c_3	a_1
F_{cg}	−1.95	−0.046	$6.6 \cdot 10^{-4}$	$-1.3 \cdot 10^{-6}$	14.1
K_f	69.88	0.009	$-3.53 \cdot 10^{-5}$	–	−1.34

	b_1	a_2	b_2	a_3	b_3
F_{cg}	−13.78	−11.22	0.1	13.04	11.58
K_f	0.54	−0.23	0.55	−0.56	1.26

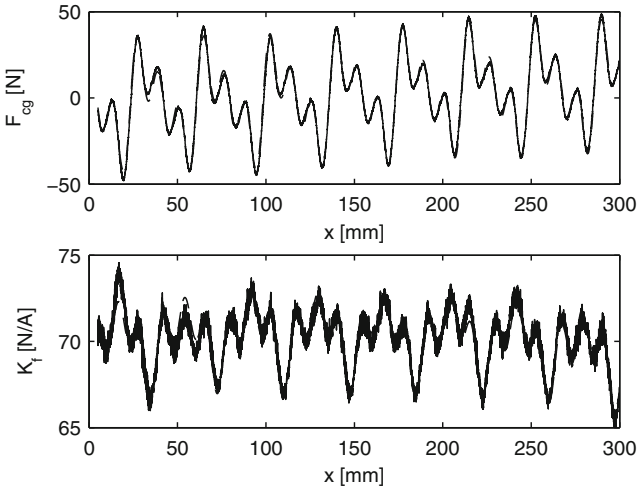

Fig. 10 Comparison between real and fitted curves

[13, 21], and the generalized Maxwell-slip (GMS) model [1, 11]. Besides accurately representing nonlocal memory, the GMS model presents improvements capturing friction lag and non-drifting behavior [11]. As mentioned earlier, friction force is described by the GMS model [1, 11, 14] in the present work.

2.4.1 GMS model

References [11, 15] describe in detail the GMS model and show different methods of friction compensation applied to ball-screw drives. In the system of the present paper, there is no ball-screw transmission, and friction only occurs at the linear guideways. The GMS model will be employed to model friction in these guideways. Although the model will be employed as shown in Ref. [11], some of the parameters will be determined in a different manner according to the particularities of the present system. These parameters are those corresponding to the Stribeck curve and parameters related to the pre-sliding regime.

A brief outline of the GMS model as described in [11] is given for self-containment, as it is required to explain the particular manner in which parameters were determined for the present system.

The GMS model can be considered as composed by a parallel arrangement of N single-state dynamic friction elements whose common input is the sliding velocity $v = \dot{x}$ and where each elementary model contributes with a force F_i to the total friction force. The total force for a N-element model results in

$$F_f(t) = \sum_{i=1}^{N} F_i(t) + \sigma_2 v(t) \tag{8}$$

where $\sigma_2 v(t)$ represents viscous friction while the first term accounts for the contribution of all single-state friction elements. A block representation of the model is shown in Fig. 11.

For every elementary model, there is a logic state indicating whether the element sticks or slips. If an element sticks, its dynamics is given by

$$\frac{dF_i}{dt} = k_i v \tag{9}$$

and the element remains in this condition until $F_i = \nu_i s(v)$. Here, k_i is the stiffness of the element and ν_i is a constant related to the contribution of this element to the total force satisfying $0 \leq \nu_i \leq 1$ and $\sum \nu_i = 1$. The function $s(v)$ is such that the friction force for a steady-state velocity v is given by $s(v) + \sigma_2 v$. The parameterization of $s(v)$ chosen in this work is also given in [11] and is as follows

$$s(v) = \text{sgn}(v)\left(F_c + (F_s - F_c)e^{-\left|\frac{v}{V_s}\right|^{\delta_{V_s}}}\right) \tag{10}$$

being F_c the Coulomb force, F_s the static force, V_s the Stribeck velocity, and δ_{V_s} the Stribeck shape factor.

On the other hand, if the element is slipping, its dynamics is given by

$$\frac{dF_i}{dt} = \text{sgn}(v)\nu_i C\left(1 - \frac{F_i}{\nu_i s(v)}\right) \tag{11}$$

where C is called the attraction parameter and the elementary model keeps slipping until velocity crosses zero.

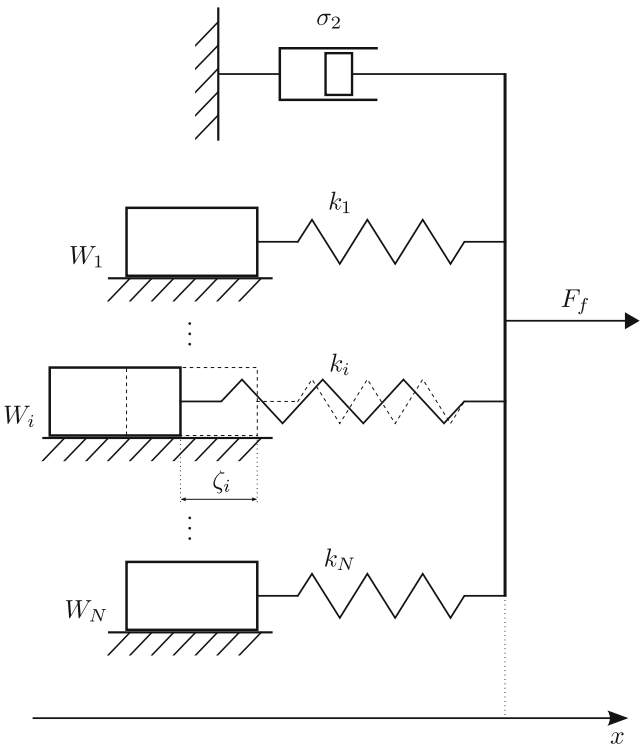

Fig. 11 Representation of the GMS model including viscous friction

It should be noted that according to the friction model, the Stribeck curve, i.e., the static relationship between steady-state velocity and friction force, is given by the following odd function of velocity

$$F_f(v) = \mathrm{sgn}(v)\left(F_c + (F_s - F_c)e^{-\left|\frac{v}{V_s}\right|^{\delta_{V_s}}}\right) + \sigma_2 v \qquad (12)$$

Reference [11] suggests an identification based on three dedicated experiments, identification of the Stribeck curve, determination of the hysteresis parameters ν_i and k_i, and calculation of the attraction parameter.

2.4.2 Stribeck curve determination

For determination of the Stribeck curve, a series of closed loop motions at constant speed along the motor stroke were performed, as done in several works [2, 11, 12, 15]. However, due to the presence of cogging, the steady-state friction force is calculated from motion in both directions, taking advantage of the odd symmetry of the Stribeck curve in Eq. 12. Thus, friction force is calculated as

$$F_f(v) = \frac{K_f(x)}{2}(I(x, v, 0) - I(x, -v, 0)) \qquad (13)$$

A number of constant speed motions were performed without load in both directions. Then, from Eq. 13, the values of $F_f(v)$ are obtained for a range of position values, adopting for $F_f(v)$ the mean along that range. Afterwards, the values of F_f for several speeds v are fitted to the expression given in Eq. 12. The resulting parameters are shown on Table 2 while Fig. 12 shows the good agreement between real data points and fitted curve.

2.4.3 Determination of the attraction parameter

As suggested in [11], parameter C is determined through a motion at variable positive speed, avoiding zero velocity in order to keep all the model elements sliding during the experiment. Under these conditions, from Eq. 11 and the derivative of Eq. 8 results

$$\frac{\mathrm{d}}{\mathrm{d}t}(F_f - \sigma_2 v) = C\,\mathrm{sgn}(v)\left(1 - \frac{F_f - \sigma_2 v}{s(v)}\right) \qquad (14)$$

Equation 1 is used to obtain F_f, from which $\frac{\mathrm{d}F_f}{\mathrm{d}t}$ is calculated. Finally, a least squares fit of parameter C in Eq. 14 results in a value of $C = 10.8$N/s.

Table 2 Stribeck curve parameters

F_s[N]	F_c[N]	$V_s\left[\frac{\mathrm{mm}}{\mathrm{s}}\right]$	δ_{V_s}	σ_2 [Ns/mm]
26.1	21.6	3.1	0.6	0.054

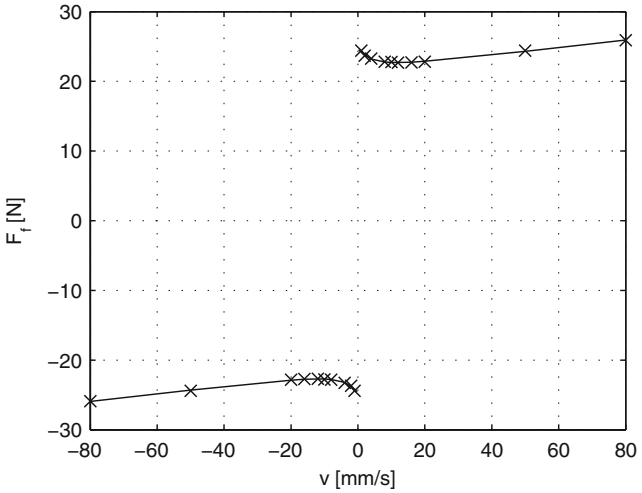

Fig. 12 Comparison between real data points and fitted Stribeck curve

It must be noted that since acceleration is not negligible, motor inertia has to be determined before calculation of C. This is done in an open-loop experiment applying a suitable force reference to the system, resulting in a mass of $m = 16.1$ kg.

2.4.4 Determination of pre-rolling parameters

Reference [11] recommends to obtain the pre-rolling parameters as for the Maxwell-slip implementation of the hysteresis function on the Leuven model. It will be assumed that velocity during the experiment is low enough as to neglect the viscous friction term and to consider $s(v) \approx F_s$. In such a case, as pointed out in [11], the GMS model reduces to the aforementioned Maxwell-slip model. Thus, as shown in [11], friction force can be expressed as

$$F_f = \sum_{i=1}^{N} W_i \Phi_i(x, \zeta_i, \Delta_i) \qquad (15)$$

where ζ_i is a redefinition of the state of element i, Δ_i is the maximum spring extension of element i, and W_i is the maximum Coulomb force for the same element, considering the model elements shown in Fig. 11. The functions Φ_i are known, and the model parameters to be determined are the W_i and Δ_i. Then, friction force depends linearly on the W_i, but not on the Δ_i. The procedure in [11] consists on pre-assigning the Δ_i along the range of pre-rolling displacement. Then, as F_f depends linearly on the W_i, these parameters can be obtained by a simple least squares fit, and from these, k_i and ν_i are calculated as

$$\nu_i = \frac{W_i}{F_s} \qquad k_i = \frac{W_i}{\Delta_i} \qquad (16)$$

Pre-assigning equally spaced values of Δ_i as suggested in [11] resulted in large negative values for some of the W_i.

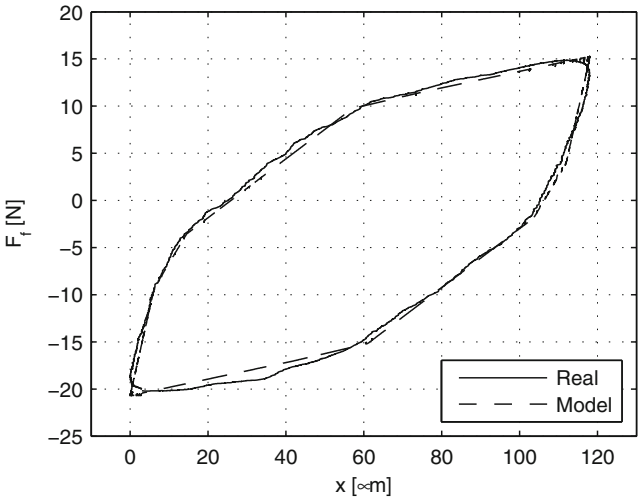

Fig. 13 Comparison between measurement and simulation for the pre-rolling regime

This is due to the error in the friction force calculated for the current system, resulting in irregularities on the shape of the force-position curve. Because of this, the Δ_i was chosen in a different manner. As done in [34], the system was excited with low-frequency periodic signals of different amplitude. The excitation with bigger amplitude was used to determine Δ_N obtained as half the distance from motion reversal to the end of pre-rolling region. On the other hand, the smaller amplitude excitation was used to determine the values of $\Delta_1, \cdots, \Delta_{N-1}$ based on the change of slope on the force-position curve. The procedure is similar to that in [34], except that the curve approximated by a piecewise linear function was the force-position curve instead of the virgin curve of the hysteresis loop. Then, the first $N-1$ nodes determined the values of $\Delta_1, \cdots, \Delta_{N-1}$ as half the distance from the motion reversal point to the manually selected knots. However, in contrast to [34], these values were then used to obtain the rest of the parameters by a least-squares fit as follows.

Applying the condition on the W_i regarding the break-away force F_s, that is $W_N = F_s - \sum_{i=1}^{N-1} W_i$, the force equation can be expressed as

$$F_f(k) - F_s \Phi_N(k) = \sum_{i=1}^{N-1} W_i(\Phi_i(k) - \Phi_N(k)) \tag{17}$$

where $W_1, \ldots, W_{N-1}$ can be determined from a least squares fit. Once obtained these values, W_N is calculated as

$$W_N = F_s - \sum_{i=1}^{N-1} W_i \tag{18}$$

and the parameters v_i and k_i are determined as in Eq. 16. Figure 13 shows the actual pre-rolling friction data in contrast to the simulated model output for the smaller amplitude excitation, while the model parameters are shown in Table 3.

3 Model performance in simulations

The model proposed in this work can be used for simulation of linear motors. Therefore, in this, section the model performance in simulations is shown compared to measured data for the actual system. Figure 14 shows measured and simulated model data for a position-controlled linear motor under a sinusoidal position reference with an amplitude of 30 mm and a 6-s period, where only the top portion of a motion reversal is considered due to its significance in the induced error evaluation. From Fig. 14a, it can be seen that the output of the complete model, that is with GMS friction and including aperiodic terms in cogging, shows a good agreement with the measured data. Now, it is possible to evaluate the contribution of the relevant submodels. For example, when the aperiodic terms are not considered in the cogging model, the error increases as can be seen in Fig. 14b. Also, there is an important error increase at points of motion reversal when friction is represented by a simple static model instead of the GMS model, as can be seen in Fig. 14c.

4 Model performance in feedforward control

As mentioned earlier, the GMS model is capable of capturing most of the observed friction phenomena. As such, it can be expected to be able to compensate most of the friction induced errors when incorporated into a feedforward term in combination with a simple linear closed loop controller. In this way, a state-space controller has been tuned, preceded by a commonly used pre-filter (ZPETC-Zero Phase Error Tracking Controller) for positioning systems [28], with a feedforward signal to compensate friction and cogging. A diagram of the control set on the system is shown in Fig. 15.

The reference is a sinusoidal with an amplitude of 5 mm and a 6-s period. Figure 16a shows the position error with

Table 3 GMS model parameters

Element	v_i	k_i $\left[\frac{\text{N}}{\text{mm}}\right]$
1	0.17	1,152.07
2	0.13	377.23
3	0.30	215.33
4	0.017	9.39
5	0.38	87.66

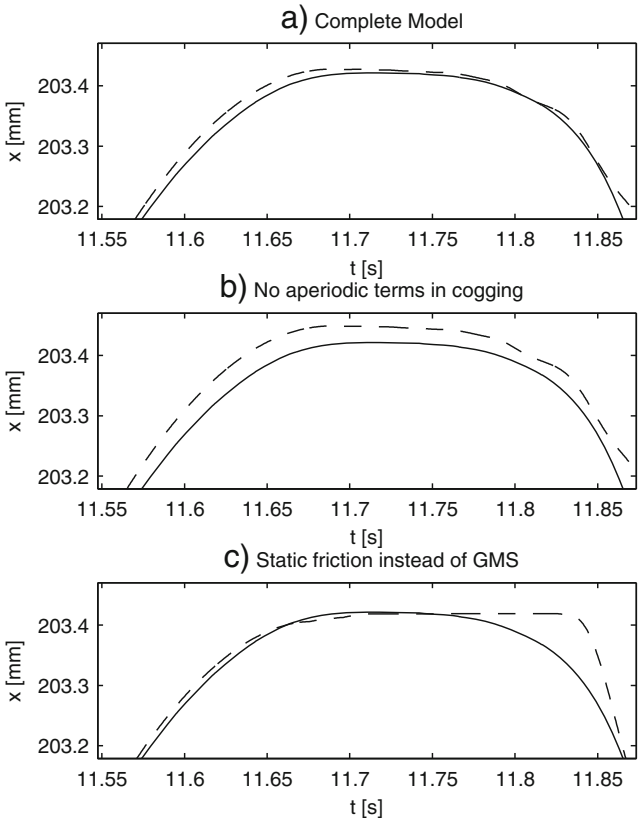

Fig. 14 Top reversal portion of a sinusoidal motion. *Solid line* measured position, *dashed line* simulation results

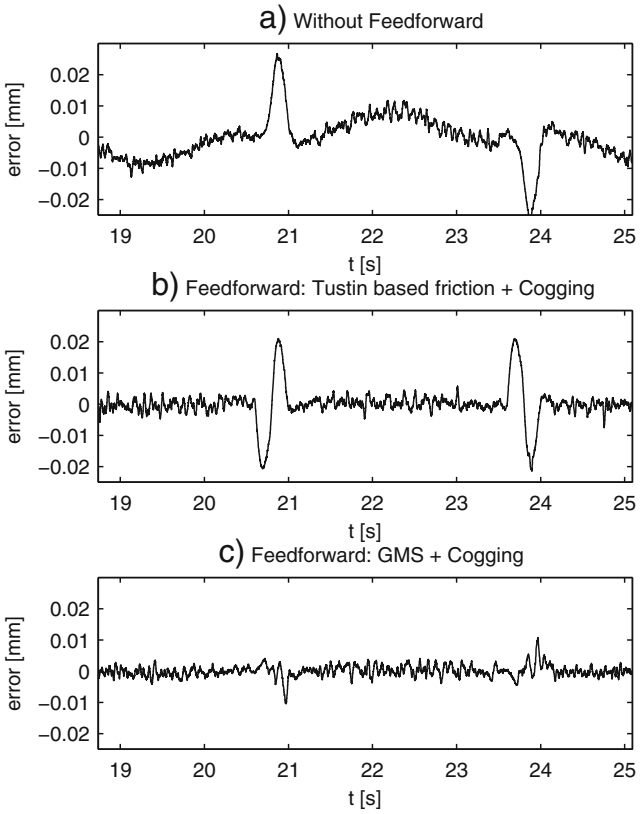

Fig. 16 Feedforward control performance

the linear controller without feedforward compensation, showing a maximum value of 27 ∝m at the motion reversal and 13 ∝m at the points of maximum velocity. After that, feedforward compensation was added but only with a Tustin-based model for friction. The parameters used for the Tustin parameterization are those previously obtained, as shown in Table 2. With this term, the error at motion reversal decreases to 23 ∝m and a second peak appears, as shown in Fig. 16b. However, the error in the area of maximum velocity was reduced to an error band of approximately ± 6 ∝m. Nevertheless, when the GMS model is used, the error at motion reversal is reduced considerably to 11 ∝m, and in most of the trajectories, the error is bounded to an error band of about ±4 ∝m, as shown in Fig. 16c. This indicates the importance of including a friction model considering the pre-rolling regime whenever performance at motion reversal is important.

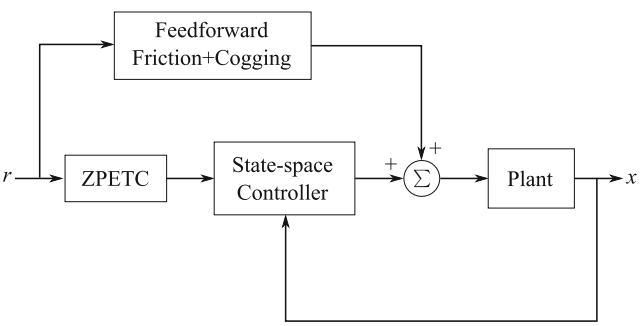

Fig. 15 Control diagram for the experiment

5 Conclusions

A model for an iron-cored PMLSM under current control is shown in this work. The model includes cogging force, ripple effect, friction, and the electrical dynamics of the current loop. Model parameters have been obtained for the present system, and model performance has been evaluated in both simulation and feedforward control. The procedure followed in the determination of the complete curves for cogging and ripple for the present system has been shown. For both curves, their frequency content was subsequently analyzed as a function of position in order to assess aperiodic variations along the motor stroke. In general, validation data shows reasonable agreement between the model and real data. The main conclusions are:

– The particular way in which the experiments at constant speed and ulterior data processing were performed in Section 2.3.1 allowed to visualize the periodic and

aperiodic behavior of cogging and ripple terms without additional measurement equipment.
- Although the cogging curve exhibits a predominantly periodic behavior, clear aperiodic behavior has also been verified. The same can be concluded about ripple except that aperiodic behavior is less significant.
- With only a few additional terms to a purely periodical model, a considerable reduction of the curve fitting error can be obtained for the cogging curve. A similar result can be obtained for ripple curves except that the improvement is less significant.
- Selecting some of the parameters (Δ_i) needed for the GMS model in the particular manner shown in Section 2.4.4 has reduced the problem of large negative values in certain parameters (W_i) required to be positive.
- The model performance at the points of motion reversal is clearly improved when using the GMS model as a result of its capability to represent pre-rolling friction.

References

1. Al-Bender F, Lampaert V, Swevers J (2005) The generalized Maxwell-slip model: a novel model for friction simulation and compensation. IEEE Trans Autom Control 50:1883–1887
2. Altpeter F (1999) Friction modeling, identification and compensation. PhD thesis, École Polytechnique Fédérale de Lausanne, Lausanne, Switzerland
3. Bascetta L, Rocco P, Magnani G (2010) Force ripple compensation in linear motors based on closed-loop position-dependent identification. IEEE/ASME Trans Mechatron 15(3):349–359
4. Canudas deWitC, Olsson H, Åström KJ, Lischinsky P (1995) A new model for control of systems with friction. IEEE Trans Autom Control 40(3):419–425
5. Chen SL, Huang S, Tan KK (2008) Relay-based force ripple and friction modeling for the permanent magnet linear motor. In: 10th international conference on control, automation, robotics and vision. ICARCV 2008. pp 2015–2019. doi:10.1109/ICARCV.2008.4795840
6. Chen SL, Tan KK, Huang S, Teo CS (2010) Modeling and compensation of ripples and friction in permanent-magnet linear motor using a hysteretic relay. IEEE/ASME Trans Mechatron 15(4):586–594. doi:10.1109/TMECH.2009.2030794
7. Dupont P, Armstrong B, Hayward V (2000) Elasto-plastic friction model: contact compliance and stiction. In: Proceedings of the American control conference. pp 1072–1077
8. Hecker R, Flores G (2008) A review of machine-tools servocontrol level. Lat Am Appl Res (Int J) 38:85–94
9. Hirvonen M (2006) On the analysis and control of a linear synchronous servomotor with a flexible load. PhD thesis, Lappeenranta University of Technology, Lappeenranta, Finland
10. Kaneko S, Sato R, Tsutsumi M (2008) Mathematical model of linear motor stage with non-linear friction characteristics. J Adv Mech Des Syst Manuf 2(4):675–684
11. Lampaert V (2003) Modelling and control of dry sliding friction in mechanical systems. PhD thesis, Katholieke Universiteit Leuven, Leuven, Belgium
12. Lampaert V, Swevers J, Al-Bender F (2002a) Experimental comparison of different friction models for accurate low-velocity tracking. In: Proceedings of the 10th mediterranean conference on control and automation
13. Lampaert V, Swevers J, Al-Bender F (2002b) Modification of the leuven integrated friction model structure. IEEE Trans Autom Control 47:683–687
14. Lampaert V, Al-Bender F Swevers J (2003) A generalized maxwell-slip friction model appropriate for control purposes. In: Proceedings 2003 international conference physics and control, 2003, vol 4. pp 1170–1177
15. Lampaert V, Swevers J, Al-Bender F (2004) Comparison of model and non-model based friction compensation techniques in the neighbourhood of pre-sliding friction. In: Proceeding of the 2004 American control conference
16. Lu L, Chen Z, Yao B, Wang Q (2008) Desired compensation adaptive robust control of a linear-motor-driven precision industrial gantry with improved cogging force compensation. IEEE/ASME Trans Mechatron 13(6):617–624
17. Nawab SH, Quatieri TF (1988) Advanced topics in signal processing, Prentice-Hall, Englewood Cliffs, New Jersey, chap Short-time Fourier transform. pp 289–337
18. Van Den Braembussche HVB J Swevers P, Vanherck P (1996) Accurate tracking control of linear synchronous motor machine tool axes. Mechatron 6:507–521
19. Prajogo T (1999) Experimental study of pre-rolling friction for motion-reversal error compensation on machine tool drive systems. PhD thesis, Katholieke Universiteit Leuven, Leuven, Belgium
20. Röhrig C, Jochheim A (2001) Identification and compensation of force ripple in linear permanent magnet motors. In: Proceedings of the American control conference
21. Swevers J, Al-Bender F, Ganseman CG, Prajogo T (2000) An integrated friction model structure with improved presliding behavior for accurate friction compensation. IEEE Trans Autom Control 4(45):676–686
22. Tan K, Zhao S (2002) Adaptive force ripple suppression in iron-core permanent magnet linear motors. In: Proceedings of the 2002 IEEE international symposium on intelligent control. pp 266–269. doi:10.1109/ISIC.2002.1157773
23. Tan K, Lim S, Huang S (1999) Two-degree-of-freedom controller incorporating rbf adaptation for precision motion control applications. In: Proceedings 1999 IEEE/ASME international conference on advanced intelligent mechatronics. pp 848–853. doi:10.1109/AIM.1999.803283
24. Tan K, Huang S, Lee T (2002) Robust adaptive numerical compensation for friction and force ripple in permanent-magnet linear motors. IEEE Trans Magn 38(1):221–228. doi:10.1109/20.990111
25. Tan KK, Lee TH, Huang S (2008) Precision motion control: design and implementation. Springer, London
26. Tanaka T, Otsuka J, Oiwa T (2009) Precision positioning control by modeling frictional behaviors of linear ball guideway. Int J Autom Technol 3(3):334–342
27. Tjahjowidodo T, Al-Bender F, Van Brussel H (2005) Friction identification and compensation in a dc motor. In: The proceedings of 16th IFAC World congress
28. Tomizuka M (1987) Zero phase error tracking algorithm for digital control. J Dyn Syst Meas Control 109:65–68
29. Xie Q, Liang SY, Chen R (2006) Modelling of linear motor feed drives for grinding machines. Int J Manuf Res 1(1):41–58
30. Xu L, Yao B (2000) Adaptive robust precision motion control of linear motors with ripple force compensations: theory and experiments. In: Proceedings of the 2000 IEEE international conference on control applications

31. Yamazaki T (2008) Mathematical model for feed drive system in microscopic motion area. Arch Mater Sci Eng 33(1): 35–38
32. Yao B, Xu L (1999) Adaptive robust control of linear motors for precision manufacturing. In: The 14th IFAC World Congress. pp 25–30
33. Yao B, Hu C, Wang Q (2007) Adaptive robust precision motion control of high-speed linear motors with on-line cogging force compensations. In: Proceedings of IEEE/ASME conference on advanced intelligent mechatronics. pp 1–6
34. Zamberi J (2008) Disturbance compensation for machine tools with linear motor drives. PhD thesis, Katholieke Universiteit Leuven, Leuven, Belgium
35. Zhu YW, Jin SM, Chung KS, Cho YH (2009) Control-based reduction of detent force for permanent magnet linear synchronous motor. IEEE Trans Magn 45(6):2827–2830